



Research Article

An Approach to Identify Regions of Interest in Chest X-Ray Images of COVID-19 Patients and Its Clinical Validation: An Indian Study

Subhagata Chattopadhyay 

Acculi Labs Pvt. Ltd. R. R. Nagar, Bangalore 560098, Karnataka, India
E-mail: subhagata.chattopadhyay2017@gmail.com

Received: 18 January 2022; **Revised:** 7 March 2022; **Accepted:** 12 March 2022

Abstract: *Background & Objective:* This study aims to develop a simple and low-cost approach in identifying the Regions of Interest (ROI) inside the lung fields and accessory structures in the respiratory system. *Methods:* To achieve this goal, Marker Based Watershedding (MBW) segmentation operation has been applied on ten Chest X-Ray (CXR) images of COVID-19 patients. CXR is economic compared to CT images and MBW is computationally simple compared to the Deep Learning (DL) techniques. Raw images have been tested for inherent noise by computing Noise Variance (NV) and Signal-to-Noise ratio (SNR). Then, 'Simple Median Filter (SMF)' was used to denoise raw images before MBW operation and the denoising performance was checked by estimating the Mean Squared Errors (MSE), and Peak Signal-to-Noise Ratio (PSNR). Regions of Interest (ROI), thus obtained, are then validated by radiologists and then clinically correlated with the symptoms. *Results:* The study shows that the SMF is an efficient filter for CXR images and MBW can identify the ROIs, which are supported by the symptoms. *Conclusion:* The paper presents a simple, low-cost (both financially and computationally), and reliable method to get a complete clinical picture of COVID-19 cases by applying the MBW segmentation technique on CXRs that is further validated with radiologists. The social implication of this work is that it can be used by general physicians and nurses in remote areas as a ready reference to important regions of the lungs, where, radiologists are unavailable. The approach can be incorporated in telemedicine during a pandemic period.

Keywords: medical image processing, medical diagnosis, telemedicine, COVID-19, watershedding image segmentation, simple median filter

1. Introduction

Coronavirus Disease 2019 (COVID-19) has been an ongoing pandemic that started in Wuhan, China in 2019 [1]. Since then, it has affected many countries irrespective of their socioeconomic status. According to World Health Organization (WHO) data, in India, from 3 January 2020 to 12:20 pm CEST, 14 May 2021, there have been 24,046,809 confirmed COVID cases and 262,317 demises, reported to WHO [2]. As per the data available on the WHO website, until 3 May 2021, a population size of 175,171,482 has vaccinated [2], which is approximately 1% of the total population at the initial time midst public dilemma [3]. Despite the best effort by the local administration, however, people are still getting infected rapidly as presently during its second wave, the virus has been mutated (double mutant

variety namely, B.1.617, with two mutations, such as the E484Q and L452R) to become more virulent, i.e., faster transmission, greater reproducibility, and higher infectivity even with lower viral load [4] and due to such mutation, it has reduced its weight and therefore developed aerosol (in-air) mode of transmission abreast contact mode of transmission [5]. Assuming the morbidity load, the Indian government, in 2020, legalized telemedicine practice in the country with guidelines for healthcare professionals [6]. Among several signs and symptoms, the most common sign of COVID-19 infection is the lung involvement leading to Ground Glass Opacity (GGO) in its lobes (40-83%) [7], which is presented with the symptoms, such as high fever, continuously wheezing type of cough, respiratory distress of various grades, severe fatigue, and fluctuating SpO2 level [8]. Therefore, Chest X-Ray or CT Chest to visualize the extent of lung involvement remains one of the mainstay investigations abreast several pathological tests, e.g., RTPCR swab test, D-Dimer, CRP, LDH, Ferritin, Procalcitonin, Neutrophil-to-Lymphocyte Ratio (NLR), etc. in blood [9].

In a medical image, anatomical structures are grossly overlapped on each other, especially in low-end modalities, such as X-Rays. Image processing is gaining its popularity in analyzing medical images and it is a popular multidisciplinary field where computer algorithms are used to compartmentalize an image in identifying the interesting regions/compartments and the anatomical structures (objects) inside and in turn segregate from its background for clinical decision making. Such compartments are called the 'Regions of Interest (ROI)' and the operation is called 'Segmentation'. ROIs, in turn, may help medical doctors to focus on these areas in addition to the other relevant areas, known as accessory regions for screening and diagnosis, determining treatment regime, and or evaluating the prognosis of any underlying illness. Due to the overlapping nature of the anatomical structures, segmentation is a challenging research area to identify the ROIs efficiently among many possibilities. Segmentation operation can be applied in various imaging modalities, such as X-Rays, Computerized Tomogram (CT), Ultra Sonogram (USG), Magnetic Resonance Imaging (MRI), functional Magnetic Resonance Imaging (fMRI), Doppler study, Fluoroscopy, Positron Emission Tomogram (PET), Single Photon Emission Computerized Tomogram (SPECT) and so forth. This work focuses on Chest X-Ray (CXR) images.

There are six classes of segmentation operations, such as a) Classical (Thresholding, Region-based and Edge-based), b) Pattern recognition-based, c) Wavelet-based, d) Deformable models, e) Artificial Neural Network (ANN) or Deep Learning (DL), and f) Atlas-based techniques in medical image processing [10, 11]. This work focuses on the Classical technique of segmentation instead of DL-based techniques, which are computationally complex [12].

Two-Dimensional Chest X-Ray (2D-CXR) is the commonest and most economical imaging modality with immense clinical significance in screening, diagnostic, therapeutic, and prognostic evaluations of any clinical condition, compared to other imaging modalities, such as CT and MRI, which are much costlier. Moreover, CXRs cause fewer radiation hazards when compared to CT and MRI and have better availability. Earlier, CXRs were developed as a film inside darkrooms, which was not only time-consuming but also artifact-prone. In the current time, digital CXRs are available at less time and with appreciable visual clarity and with fewer artifacts. COVID-19 cases are steadily rising in the population and hence the volume of radiological images is growing proportionally. On the other hand, the number of radiologists scores less compared to the catering population, especially in the developing nations and their remote areas. This is an inherent challenge in any healthcare sector to manage this rising volume of CXR images by timely and accurately interpreting its findings. This responsibility is now mostly on the General Physicians (GPs), who do not have any formal training as radiologists; however, can read X-Ray plates with variable confidence. Given some assistance, the GPs would read these plates with higher confidence and better accuracies. To address this shortfall, technology has been brought as the assistive tool to them in the current imaging research. Summarily, such assistance is aimed to prevent 'under' or 'over' diagnosis.

In the following section, a summary of the relevant literature shows how various segmentation techniques are applied in various medical imaging modalities, such as mammograms, CT, MRI, X-Rays, PET, USG, Nuclear Imaging, etc. Due to space constraints, all studies cannot be cited in this work.

2. Literature review

For four decades, active research is going on for efficient segmentation operations in image analysis [13, 14]. Medical image segmentation is a continuously evolving research field [15, 16] as a potential sub-field of medical image

processing [17, 18]. Various studies showcase several types of segmentation operations applied on different X-Ray modalities. Below, Table 1 depicts a list of studies and provides the intensity and depth of the research in this area. It is important to note that this is not an exhaustive list. Many other relevant studies are reported in various journals, conferences, and chapters in books of international repute, which could not be cited here due to the space constraint.

Table 1. Summary Literature survey on the segmentation operations in medical images

Author and Year (citation)	Image modality	Segmentation technique	Observation
[19]	Mammogram	Global Thresholding	Efficient in detecting tumorous and normal breast tissue. However, as most medical images are not bimodal, thresholding is rarely used in medical image processing.
[20]	CT, Nuclear imaging, USG, MRI	Adaptive Thresholding	Efficient when used with an Insight Toolkit, comprising of statistical pattern mapping, Hidden Markov Model, PDE-based non-linear image filtering, etc.
[21]	CT, PET, MRI	Several segmentation methods, such as Thresholding, Contour detection, ROI, and so on	Applying a single segmentation technique might not be a good idea for segmentation.
[22]	Bone X-Ray	Region-based segmentation (Watershed method)	A useful technique to identify ROIs. However, over-segmentation and being influenced by noise are two drawbacks of this technique.
[23]	X-Ray Hand and Wrist	Region-based segmentation	Able to identify conjugated bones in the wrist.
[24]	Various medical Images	Edge detection techniques (including Sobel, Prewitt, Roberts, or Canny detectors)	All are found efficient.
[25]	Various medical images	Edge detection techniques (including Sobel)	All are found efficient.
[26]	X-Ray	Edge detection techniques (including Sobel, Prewitt)	Efficient in detecting fractures in the bone.
[27]	X-Ray	Edge detection techniques (including Sobel and Roberts or Canny detectors)	Able to evaluate the prognosis of total hip replacement by locating the prosthetic material and the bone. The canny detector was found most efficient.
[28]	X-Ray	Pattern recognition-based (clustering)	Appropriate for the multi-brand images and the color images, although detecting an optimum number of clusters is a tedious task.
[29]	X-Ray	Pattern recognition-based (classification)	Adaptive fuzzy index measure is a useful approach for image segmentation.
[30]	X-Ray	Deformable models (Active contour or snakes)	Able to detect the fracture line in low contrast X-Ray images efficiently. Does not work well where the curves and bends are sharper in the image.
[31]	X-Ray and MRI	Deformable models (level set method)	Able to handle noise, intensity inhomogeneity in a low-quality medical image.
[32]	X-Ray (vertebrae)	Deformable models (active shape model)	A combination of Canny edge detection, Harris corner detection, and filtering techniques performs very well in detecting the corners of the vertebrae under examination.
[33]	X-Ray (dental caries)	Wavelet-based and Dual-Tree Complex Wavelet Transform method	Able to identify the residue caries post Root Canal Treatment (RCT) to evaluate the accuracy of the RCT procedure done by the dentist.
[34]	X-Ray (Chest)	Atlas-based method	Robust with an accuracy of about 95% in the automatic diagnosis of images.
[35]	X-Ray (Chest)	Knowledge-based technique	The algorithm was able to detect lung boundaries and abnormalities with 88% sensitivity and 95% specificity.
[36]	CT (Chest) COVID-19 affected patients	Artificial neural nets	U-Net and VB-Net methods performed well in image segmentation for automatic detection of ground-glass opacity in lung fields.
[37]	X-Ray (Chest) COVID-19 affected patients	Bio-inspired hybrid methods (Chaotic Salp Swarm algorithm, Deep learning methods, and 2D Curvelet Transform)	Diagnosis of COVID-19 was highly rapid and accurate.

Research gap & Objective: To date, to the best of the knowledge, no research has been reported that has pursued the development of a low-cost, simple segmentation operation to identify the ROIs of CXR pictures, which is economic compared to CT scanning of COVID-19 patients, then radiologically validated and in turn, clinically correlated the ROIs, thus obtained, to obtain the complete clinical picture.

The rest of the paper is organized as follows. Section III describes the Material and Methods; Results are shown in Section IV, while in Section V a detailed discussion has been made on the results; Section VI concludes the paper and shows some research areas as the extension of this work in the future.

3. Materials and methods

In this section, the material under study (here adult CXR images) and various methods, under which there are various approaches and techniques, applied in this work, are discussed.

3.1 Material

The material under this study is as follows:

- COVID-19 (RTPCR +ve) CXRs (.png, .jpg)
- Adult males and females, 5 each
- Steroid and Antibiotics-naïve
- Symptoms recorded for clinical correlations
- Variable comorbidities (all under medication and controlled)

Table 3 under Section IV has showcased each complete case (i.e., validated and clinically correlated ROIs).

3.2 Method

Step-1: Noise estimation of raw images by computing

- Noise Variance (NV)
- Signal-to-Noise Ratio (SNR)

Step-2: Denoising images using Simple Median Filter (SMF)

Step-3: Comparing the quality of original and denoised images by measuring

- Mean Squared Error (MSE)
- Peak Signal to Noise Ratio (PSNR)

Step-4: Applying Marker-based Watershed (MBW) thresholding operations on denoised images to Identify ROIs, and

Step-5: Validating ROIs radiologically and corroborated clinically to get a complete picture of a COVID-19 case.

Below, the working principles and theoretical foundations of the approaches and techniques, mentioned under ‘Method’ are discussed briefly.

3.2.1 Step-1 Noise estimation in raw images

Noise estimation in raw images is one the most important steps in image processing, as all images are naturally noisy. Noise occurs during acquisition, coding, transmission, and processing in the imaging technique [38]. In this work, two popular estimators of noise, such as the Noise Variance (NV) and Signal-to-Noise Ratio (SNR) are applied [38]. Their working principles are explained below.

Noise Variance (NV)

If an image $f(i, j)$ is scaled by additive terms ‘ a ’ and ‘ b ’, to give

$$g(i, j) = af(i, j) + bf(i, j) \quad (1)$$

If an image $f(i, j)$ is scaled by multiplicative factor 'a' and 'b', to give

$$g(i, j) = af(i, j) \times bf(i, j) \quad (2)$$

In this study, an additive term have been used as follows,

$$g(i, j) = af(i, j) + b \quad (3)$$

then, mean of $g(i, j)$ is given by,

$$g = af + b \quad (4)$$

then, the variance of $g(i, j)$ is given by,

$$\sigma_g^2 = a^2 \sigma_f^2 \quad (5)$$

Where, σ_f^2 is the noise variance of image $f(i, j)$. Therefore, the value decreases with a low noise level. After computing the noise variance, Signal-to-Noise Ratio (SNR) has been computed, as follows.

Signal-to-Noise Ratio (SNR)

$$f(i, j) = s(i, j) + n(i, j) \quad (6)$$

then, variances of $s(i, j)$ and $n(i, j)$ can be written as

$$\sigma_s^2 = \left\{ |s(i, j) - s(i, j)|^2 \right\}, \text{ and} \quad (7)$$

$$\sigma_n^2 = \left\{ n(i, j)^2 \right\}, \quad (8)$$

and then SNR can be written as,

$$SNR = \frac{\sigma_s}{\sigma_n}. \quad (9)$$

Therefore, *SNR* is a ratio of true signal (*s*) and additive noise (*n*). The value increases with retention of signal against low noise level.

3.2.2 Step-2: Denoising with SMF (kernel 5×5)

SMF (type: non-linear filter, under the class Spatial filter) is a 'canonical image processing operation' and is useful in many practical applications [39]. Here the output value is calculated based on the median value of the input sample and then sorted across the data. It is a popular preprocessing step for later processing of the image, such as edge detection, segmentation, and so on. In this technique, the gray level of each pixel is at first computed and then replaced by the median value obtained from the neighborhood pixels for a given size of the kernel. The robustness of the Median filter lies in the fact that any single unrepresentative pixel in the neighborhood cannot affect the median value, but can affect the mean value. The study showed that the Median filter is much useful to reduce the Poisson type of noise that

occurs due to random bit error in a communication channel and is commonly found in medical X-Ray images [40]. For all pixels in a neighborhood of ‘w’, the following equation can express the working principle as,

$$I(k, l) = \text{median}\{x(i, j), (I, j) \in w\} \quad (10)$$

‘ $I(k, l)$ ’ represents the image obtained after filtering; ‘ $x(i, j)$ ’ are the pixels with ‘ (i, j) ’ coordinates; ‘w’ is the location, which is centered around location (k, l) of the image.

3.2.3 Step-3 Denoising performance check

Measuring the performance of a denoising technique is another important step in image processing. An appropriately denoised image leads to accurate processing. In this work, two popular denoising performance checkers, such as Mean Squared Error (MSE) and Peak Signal-to-Noise Ratio (PSNR) has been applied [41]. Below, their working principle is explained.

Mean Squared Error (MSE)

It represents the cumulative squared error between the denoised and original image (refer to equation 11). Hence, lower values are appreciated.

$$MSE = \frac{1}{m \times n} \sum_{i=0}^{m-1} \sum_{j=0}^{n-1} (I(i, j) - K(i, j))^2 \quad (11)$$

where, ‘ m, n ’ represents image matrix ‘ $I(I, j)$ ’ (original image) and ‘ $K(i, j)$ ’ (denoised image).

Peak Signal-to-Noise Ratio (PSNR)

It represents the peak error of an image and is expressed as a ratio of peak or maximum signal value and the power of the distorting noise effect. Therefore, higher values are appreciated.

$$PSNR = 20 \times \log_{10} \left(\frac{MAX}{\sqrt{MSE}} \right) \quad (12)$$

where MAX is the peak/maximum value of any pixel and MSE is the Mean Squared Error among pixels of original and denoised images. As we will see later in Section 4, Table 2 demonstrates the performance of the denoising techniques on original images by estimating MSE and PSNR.

3.2.4 Step-4 Image segmentation with Marker-Based Watershed (MBW) Operations to obtain ROI

The Watershed method of segmentation is a region-based method that follows the principles of Mathematical Morphology and exploits the virtue of the suitable combinations of two popular operations, such as ‘erosions’ and ‘dilations’ for filtering binary images [13]. Such combinations can eliminate a few objects within the image and at the same time, can retrieve some without much data loss by utilizing the property of shape of the objects within the image [42]. The original concept was introduced by Digabel and Lantuejoul in the year 1978 [14]. The practical application of the algorithm had been implemented by Vincent and Soille in 1991 [43]. Post this work, the Watershed algorithm has been used widely in medical image segmentation tasks [44]. According to Preim and Botha [44], an image is regarded as a topographic landscape with valleys and ridges (refer to Figure 1). The elevation values in the landscape refer to gray value pixels and their gradient scale. Watershed transform segments an image into catchment basins. A catchment basin comprises all points whose path of gradient descent terminates into the local minima. Watershed can decompose an image completely and assign each pixel as either a watershed or a region. Hence, in the case of noisy or raw medical data, it can generate a large number of small regions, which is popularly called the ‘problem of over-segmentation.

Gradient image is the most widely used approach as the variant of Watershed transform. It is highly sensitive to the image noise and hence appropriate denoising of the image is required. MBW operations efficiently mark the Region of Interest (ROI) in any image, even more accurately than various popular classifiers and Deep Learning (DL) techniques, such as Convolutional Neural Network (CNN) or Fuzzy c-means clustering techniques [12]. Another major advantage of MBW over other current sophisticated segmentation techniques is that it has minimum computational complexity [12].

3.2.5 Step-5 ROIs: its radiological validation and clinical correlation

COVID-19 virus predominantly infects the lungs, causing inflammation called Pneumonitis and its various sequels [8]. Hence, lung fields and their accessories that are responsible for the respiratory system are the principal areas under a CXR examination. The lung field can be divided into two sides, such as the Left (Lt) lung which has two lobes, one Upper Lobe (UL) and the other one is the Lower Lobe (LL); while the Right (Rt) lung possesses three lobes, e.g., Upper Lobe (UL), Middle Lobe (ML) and Lower Lobe (LL). Under accessory structures, the important issues are (i) the lymphatic system (called Hilar lymphatics, through which the virus spreads), (ii) trachea (air tube through which air enters into the lungs) and its position, (iii) diaphragm, which is a robust muscular structure under the lungs that moves up and down and thus allows lungs to deflate and inflate, respectively during respiration and acts as a mechanical ventilator. The shape of the diaphragm called the (iv) dome of the diaphragm is another radiologically important feature as it gives the idea of its muscular tone. Next is the (v) angle between the LLs of the lungs and diaphragm, called the Costophrenic (CP) angles, which is ideally an acute angle and is obliterated in various pathological conditions of the lungs. Thus, these structures along with the lung fields are the key ROIs, which are assessed during the radiological examination of a CXR image to screen, diagnose and make the prognosis of the respiratory system (refer to Figure 1). All these mentioned regions have a high degree of radiological importance in the screening and grading of a COVID-19 infection [45]. It is important to mention here that for getting a clearer view of these structures, Postero-Anterior (PA) views are taken during X-Ray exposure.

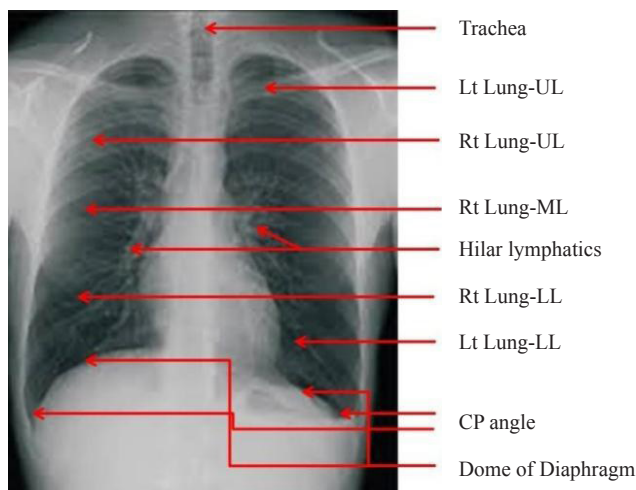


Figure 1. ROIs in a CXR for COVID-19 cases

Here, ROIs thus obtained after segmentation operation on denoised images, are clinically validated by experienced radiologists and corroborated with the symptoms of the patients, they presented with, for obtaining an overview of the cases. It is important to note that the radiologists, who took part in this study, were divided into two groups. Group I consisted of two radiologists (average experience of 21.6 years), who were not told that the CXRs belong to COVID-19 patients to avoid possible ‘over-diagnosis’. This is called as ‘blind’ approach. On the other hand, to prevent ‘under-diagnosis’, another set of radiologists (Group II) were consulted, who were divulged the fact. This is called the ‘open’

approach. Put together, this sampling method called as ‘blind and open’ approach was able to reduce the diagnostic bias. Clinical correlation of the radiological findings has been conducted with the help of a senior Internal Medicine specialist.

4. Results

In this section, results obtained from experiments are shown. Detail discussion of the results is made in the next section.


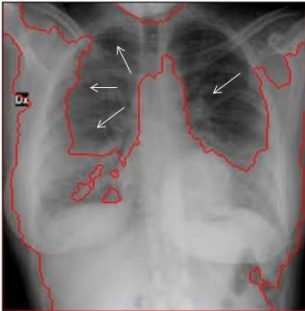

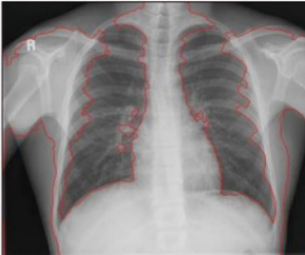

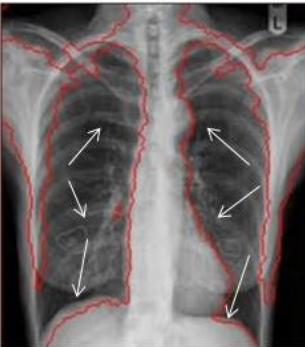

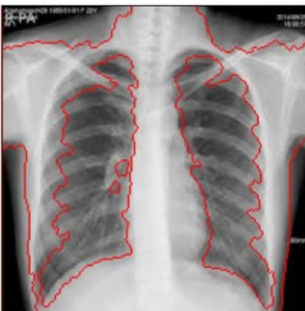
The raw CXRs have been estimated for noise within by computing Noise Variance (NV) and Signal-to-Noise Ratio (SNR). Following that, an attempt has been made to reduce the noise using a Simple Median Filter (SMF). The filtered images are then compared with their respective raw images by measuring Mean Squared Errors (MSE) and Peak Signal-to-Noise Ratio (PSNR). The combined results can be seen in Table 2.

Table 2. The noise calculation in original images and denoising performance of SMF

	Original		SMF Applied	
	NV	SNR (avg.)	MSE	PSNR
CXR-1 (226, 223)	0.0991	3.1646	3.0708	42.9548
CXR-2 (417, 500)	0.0988	3.2435	5.9408	35.5003
CXR-3 (248, 203)	0.0994	2.1749	17.6307	33.0715
CXR-4 (240, 198)	0.0998	3.0861	18.4365	34.1557
CXR-5 (248, 203)	0.0995	4.218	14.0514	35.598
CXR-6 (225, 225)	0.0999	3.0824	18.4365	34.1557
CXR-7 (194, 259)	0.0991	4.8114	6.1133	39.4771
CXR-8 (193, 261)	0.0993	4.762	14.9938	34.5796
CXR-9 (138, 130)	0.0985	3.8901	10.9929	34.1479
CXR-10 (135, 144)	0.0981	3.9011	11.934	33.7625
Mean	0.0991	3.6334	12.1600	35.7403
Standard deviation (σ)	0.0005	0.8328	5.5736	3.0917

Table 3 shows denoised CXRs (PA view) and the corresponding MBW-based ROIs, case-wise. The ROIs were in turn radiologically validated (Rad_val), the abnormal or pathological regions, which have been mentioned by the radiologists during validation, are marked with arrows in the MBW-based ROIs. These are then Clinically (Symptom-wise) correlated (Symp_corr) to obtain complete pictures of each COVID-19 case. The ‘day’ mentioned in the table refers to the number of days of the illness when the CXRs are taken. The findings of each case have also been corroborated with current literature.

Table 3. Validation of the CXRs

Denoised CXR & MBW-based ROI		Rad_val	Symp_corr
Case 1	ROI		
		Findings: Diffuse consolidation (white patches) can be seen in Rt lung (all lobes) and Lt lung (mid-lower zone). Impression: COVID-19 pneumonitis [45].	Findings: Continuous high fever × 7 days; Productive cough × 3 days; Respiratory distress × 2 days. Impression: Moderate to severe COVID-19.
Female; 48 yrs.; T2DM & COPD; 7 th day			
Case 2	ROI		
		Impression: No Abnormality Detected (NAD)	Findings: mild fever × 2 days; Generalized malaise; Weakness; Occasional dry cough × 3 days. Fully recovered. Impression: Mild COVID-19.
Female; 52 yrs.; No comorbidity; 5 th day			
Case 3	ROI		
		Findings: Emphysematous changes in both lungs; Domes of the diaphragm are flattened on both sides. Impression: Emphysema due to COVID-19 [46].	Findings: Severe dry cough × 3 days; Respiratory distress × 4 days. Impression: Moderate-to-severe COVID-19.
Female; 50 yrs.; T2DM & HTN; 4 th day			
Case 4	ROI		
		Impression: No Abnormality Detected (NAD)	Findings: mild fever × 3 days; Generalized malaise; Weakness. Fully recovered. Impression: Mild COVID-19.
Male; 48 yrs.; No Comorbidity; 6 th day			

Case 5

ROI



Findings: Prominent hilar shadow (most probably due to underlying hilar lymphadenopathy) noted on both sides.
Impression: This could be due to COVID-19 lymphadenitis [47].

Findings: No symptoms.
Impression: asymptomatic COVID-19.

Male; 42 yrs.; HTN & CAD; 8th day

Case 6

ROI



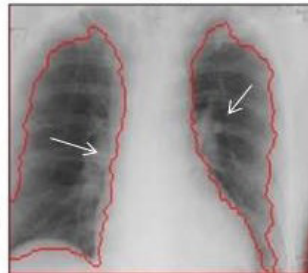
Findings: Bilateral accentuation of bronchovascular markings; Hilar vessels are prominent.
Impression: This could be an early sign of COVID-19 induced pneumonitis, which is not yet established.

Findings: No symptoms.
Impression: asymptomatic COVID-19.

Female; 47 yrs.; T2DM; 10th day

Case 7

ROI



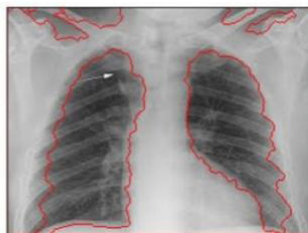
Findings: Prominent bilateral Hilar soft tissue shadows.
Impression: This could be due to COVID-19 induced hilar lymphadenopathy [48].

Findings: No symptoms.
Impression: asymptomatic COVID-19.

Male; 51 yrs.; T2DM & HTN; 11th day

Case 8

ROI



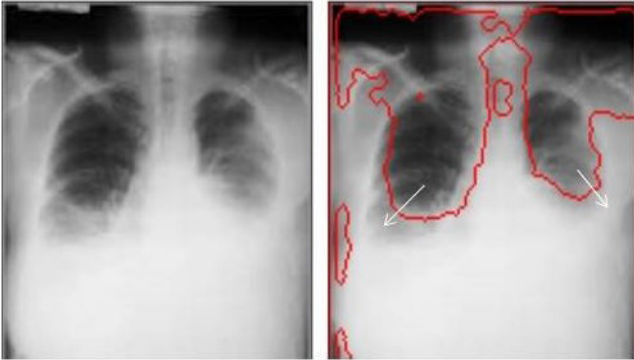
Findings: Mild dilatation of Azygous vein; Prominent superior mediastinal shadow at Rt upper region.
Impression: anatomical anomaly and may not be related to COVID-19.

Findings: No symptoms.
Impression: asymptomatic COVID-19.

Male; 46 yrs.; HTN; 9th day

Case 9

ROI



Findings: bilateral mild pleural effusions; collapsed-consolidation basal segments of both lungs.
Impression: moderate-to-severe COVID-19 pneumonia [49].

Findings: Continuous high fever × 7 days; Dry cough × 7 days; Respiratory distress × 7 days; Chest pain on both sides × 4 days.
Impression: Moderate-to-severe COVID-19.

Female; 58 yrs.; HTN, T2DM & COPD; 10th day

Case 10

ROI



Findings: Lt-sided moderate pleural effusion.
Impression: severe COVID-19 pneumonia [49].

Findings: High fever × 3 days; Dry cough × 7 days; Respiratory distress × 3 days; Chest pain × 4 days.
Impression: Severe COVID-19.

Male; 56 yrs.; T2DM & COPD; 10th day

In the next section, the findings are discussed. Supporting studies have been cited for the credibility of the findings and interpretations.

5. Discussions

The essence of this work is to develop a low-cost, simple but reliable, and replicable approach to obtain the complete clinical picture of a COVID-19 case through radiological validations and clinical correlation, especially in the developing nations where CT scanning facility is not ubiquitous and unaffordable by the common men. It would be a potential extension of the aim of telemedicine that is to cater healthcare to the maximum population without much mobility, i.e., pervasively. The terms low-cost and simple are referred to the use of CXR, instead of CT scan, which is multiple times costlier than CXR. A high-quality digital CXR costs approximately INR 200/- to 300/- to the patient and is available in Indian suburbs [50]. On contrary, a CT Scan of the Chest (CTC) costs around INR 3000/- to 3500/-, which is costly to afford by the common people and also not readily available in all the suburban radiology centers [51]. Low cost also refers to the tool's computational cost, which is quite high in Deep Learning (DL)-based segmentation operations due to its complex architecture and the computational time [52]. Compared to the DL-based segmentation approach, ROI-based segmentation using MBW is simple and easier to implement [53]. It may be noted that both the accuracy and processing time are superior to the currently used sophisticated DL-based techniques due to less cumbersome architecture and computational time complexity [12].

The reliability of a system/tool depends on its (i) user-friendly structure, (ii) easy implementation, (iii) free from clinical bias, and (iv) accuracy, which can provide a 360-degree picture of a given case. In this work, the reliability

largely depends on the quality of denoising by SMF technique, which is used in the raw images, which are inherently noisy due to error in exposure, the posture of the patient, conductivity, possible defects in the sensors, and many other conditions. It is worth noting that SMF works best on Poisson type of noise, which is predominantly found in X-Ray images [40]. Table 2 shows the noise levels in the raw images by estimating NV (average = 0.09915 and $\sigma = 0.000562$) and SNR (average = 3.63341 and $\sigma = 0.8328594$) and after SMF has been applied by computing the corresponding MSE and PSNR. Results show that SMF is able to denoise these images efficiently (MSE: average = 12.16007 and $\sigma = 5.573679$; PSNR: average = 35.74031 and $\sigma = 3.091738$). Further, the reliability has been examined while validating the ROIs by the radiologists. The quality of the ROIs depends on the accurate implementation of MBW operations on the images. The findings, thus identified through ROIs, are then radiologically validated using a ‘blind and open’ sampling approach, mentioned in Section III under Step-5. The radiological findings are then clinically correlated with the symptoms with which the patients presented. It is important to note that MBW can mark the ROIs of each CXR (refer to Table 3); however, it is not working as a typical classifier, which differentiates abnormalities within the structures. Table 3 showcases the comprehensive picture, ranging from MBW operations on denoised images to clinical correlations through radiological validations. In Table 3, it may be noted that all COVID-19 patients are not been presented with abnormal radiological findings, e.g., in cases 2 and 4. Many, on the other hand, are asymptomatic though had radiological pathologies, as found in cases 6 to 8. Associated comorbidities make patients more vulnerable to developing moderate to severe COVID in a short time, as found in cases 1, 3, 9, and 10. Hence, from these findings, it may be stated that the severity of the illness has got no direct relationship with the radiological findings at all times. The variations are due to the degrees of viral loading during transmission, its replication rate inside the cells, and the innate immunity of the infected person that pauses or stops further viral replication [54]. In the given non-linear scenario of COVID-19, the MBW-based ROIs are simple identifiers, quite informative in showing the lung fields and the accessory structures of the respiratory system by marking these. The algorithm is easy-implementable with low computational cost and also accurate in marking the ROIs in the CXR images, as validated by the radiologists. It throws useful light on the structures, which could be interesting to the radiologists and GPs or nurses for its validation and in turn, the clinical correlation for connecting the dots by assessing the symptomatic loads in COVID-19 morbidity.

The replicability of a tool depends on the technical simplicity and generic nature, which are also two salient features of this proposed approach. A user-friendly interface, which is in progress, could be useful in this aspect. The said tool can be much helpful for novice doctors, GPs, nurses where radiologists are unavailable. In this case, a classifier can be developed and used for automatic detection of abnormal structures, which MBW-based ROIs provide after analyzing an X-Ray image.

6. Conclusions and future research

The work proposes a low-cost, simple, reliable, user-friendly approach to finding interesting regions in the CXRs of a set of COVID-19 patients in the Indian scenario. MBW-based segmentation operation has been successfully applied to obtain the marked ROIs in the lung fields and the accessory structures of the respiratory systems as guidance to radiological validation and clinical correlation of each case to get a complete picture of lung infection due to the coronavirus. Before MBW application, necessary pre-processing has been done to reduce the noise in the raw images by applying the SMF and the image quality has been appreciated by the radiologists who can diagnose the pathology without difficulties; rather, MBW-based ROIs are the ready-reckoner to them. High PSNR and low MSE values corroborate the efficiency of the SMF technique. The ‘Blind and open’ sampling approach has reduced the validation bias of the study. The future work comprises of developing a GUI, where MBW-based ROIs can be predicted for any abnormalities by a classifier to completely automate the process, which could be useful to GPs, nurses, novice radiologists, especially in the developing nations and its remotest parts.

Conflict of interest statement

The author states that there is no known conflict of interest of personal, financial or organizational in this work.

References

- [1] Zhu N, Zhang D, Wang W, Yang B. A novel coronavirus from patients with pneumonia in China. *New England Journal of Medicine*. 2020; 382(8): 727-733.
- [2] World Health Organization. 2021. Available from: <https://covid19.who.int/region/searo/country/in> [Accessed 14th May 2021].
- [3] Chattopadhyay S, Shinha P. Understanding factors impacting covid vaccination in India: A preliminary report. *Quantum Journal of Medical and Health Sciences*. 2021; 1(3): 18-31.
- [4] Livemint. India's 'double mutation' covid virus variant is worrying the world. 2021. Available from: <https://www.livemint.com/news/india/indias-double-mutation-covid-virus-variant-is-worrying-the-world-11618789603145.html> [Accessed 14th May 2021].
- [5] Joshi SR. COVID 19 in India: waves, variants of concern, airborne transmission. *The Journal of the Association of Physicians of India*. 2021; 69(5): 11-13.
- [6] Central Drugs Standard Control Organization. *Directorate General of Health Services. Ministry of Health & Family Welfare*. Government of India. 2020. Available from: <https://cdsco.gov.in/opencms/opencms/en/Clinical-Trial/Ethics-Committee/Ethics-Committee-Registration/> [Accessed 30th December 2021].
- [7] Shirani F, Shayganfar A, Hajiahmadi S. COVID-19 pneumonia: a pictorial review of CT findings and differential diagnosis. *Egyptian Journal of Radiology and Nuclear Medicine*. 2021; 52(1): 1-8. Available from: doi: 10.1186/s43055-021-00415-2.
- [8] Darwish HS, Habash MY, Habash WY. COVID-19 viral pneumonia complicated with acute pulmonary embolism: A descriptive study. *Radiology Research and Practice*. 2021.
- [9] Goudourisa ES. Laboratory diagnosis of COVID-19. *Journal of Pediatrics (Rio J)*. 2021; 97(1): 7-12.
- [10] Zharkova V, Ipson S, Abouardham J, Bentley B. Survey of image processing techniques. *EGSO Internal Deliverable*. 2002.
- [11] Stolojescu-Crisan C, Holban S. A comparison of X-ray image segmentation techniques. *Advances in Electrical and Computer Engineering*. 2013; 13(3): 85-92.
- [12] Sarma R, Gupta YK. A comparative study of new and existing segmentation techniques. In *IOP Conference Series: Materials Science and Engineering*. 2021; 1022(1): 012027.
- [13] Serra J. *Image Analysis and Mathematical Morphology*. New York: Academic Press; 1982.
- [14] Digabel H, Lantuejoul C. Iterative algorithms. In *Proceedings of the 2nd European Symposium Quantitative Analysis of Microstructures in Material Science, Biology and Medicine*. 1978.
- [15] Yue Z, Goshtasby A, Ackerman L. Automatic detection of rib borders in chest radiographs. *IEEE Transactions on Medical Imaging*. 1995; 14: 525-536.
- [16] Toriwaki J, Ji T, Ji H. Computer analysis of chest photofluorograms and its application to automated screening. *Iyō denshi to seitai kōgaku. Japanese Journal of Medical Electronics and Biological Engineering*. 1980; 3: 63-81.
- [17] Chattopadhyay S. Towards grading chest X-rays of COVID-19 patients using a dynamic radial basis function network classifier. *Artificial Intelligence Evolution*. 2021; 2(2): 81-95. Available from: doi: 10.37256/aie.2220211125.
- [18] Chattopadhyay S. A novel approach to detect abnormal chest X-rays of COVID-19 patients using image processing and deep learning. *Artificial Intelligence Evolution*. 2021; 2(2): 23-41. Available from: doi: <https://doi.org/10.37256/aie.222021977>.
- [19] Pham DL, Xu C, Prince JL. Current methods in medical image segmentation. *Annual Review of Biomedical Engineering*. 2000; 2(1): 315-337.
- [20] Yoo TS. *Insight Into Images Principles and Practice for Segmentation, Registration, and Image Analysis*. In: A. K. Peters Wellesley (ed.). Massachusetts: LHNBC; 2004.
- [21] John NW. Segmentation of radiological images. In: Neri E., Caramella D., Bartolozzi C. (eds.). *Image Processing in Radiology. Medical Radiology (Diagnostic Imaging)*. Berlin, Heidelberg: Springer; 2008. p. 45-54.
- [22] Kasmir Raja SV, Shaik Abdul Khadir A, Riaz Ahamed SS. Moving toward region-based image segmentation techniques: a study. *Journal of Theoretical and Applied Information Technology*. 2009; 5: 81-87.
- [23] Manos GK, Cairn AY, Rickets IW, Sinclair D. Segmenting radiographs of the hand and wrist. *Computer Methods and Programs in Biomedicine*. 1993; 43(3-4): 227-237.
- [24] Kulkarni M. *X-ray Image Segmentation Using Active Shape Models*. Cape Town; 2008.
- [25] Tirodkar AA. A multi-Stage algorithm for enhanced X-ray image segmentation. *International Journal of Engineering Science and Technology*. 2011; 3(9): 7056-7065.

- [26] Shah S, Sharma P. Bone segmentation from X-ray images: Challenges and techniques. *Information Systems Design and Intelligent Applications*. 2018; 672: 853-862. Available from: doi: 10.1007/978-981-10-7512-4_84.
- [27] Florea L, Florea C, Vertan C, Sultana A. Automatic tools for diagnosis support of total hip replacement follow-up. *Advances in Electrical and Computer Engineering*. 2011; 11(4): 55-62.
- [28] Liang J, Abidi BR, Abidi MA. Automatic x-ray image segmentation for threat detection. In *Proceedings of the Fifth International Conference on Computational Intelligence and Multimedia Applications*. China: Xi'an; 2003.
- [29] El-Feghi I, Huang S, Sid-Ahmed MA, Ahmadi M. X-ray image segmentation using auto adaptive fuzzy index measure. In *Proceedings of the 47th Midwest Symposium on Circuits and Systems*. MWSCAS'04. IEEE; 2004. p. 499.
- [30] Jiang Y, Meng J, Babyn P. X-ray image segmentation using active contour model with global constraints. In *IEEE Symposium on Computational Intelligence in Image and Signal Processing*. 2007.
- [31] Cui WC, Wang Y, Lei T, Fan YY, Feng Y. Level set segmentation of medical images based on local region statistics and maximum a posteriori probability. *Computational and Mathematical Methods in Medicine*. 2013.
- [32] Benjelloun M, Mahmoudi S, Lecron F. A framework of vertebra segmentation using the active shape model-based approach. *International Journal of Biomedical Imaging*. 2011.
- [33] Krithiga R, Lakshmi C, Nithya A. Segmentation of dental caries from dental X-ray images using wavelet and watershed transforms. *International Journal of Applied Engineering Research*. 2014; 9(20): 4617-4624.
- [34] Candemir S, Jaeger S, Palaniappan K, Musco JP, Singh RK, Xue Z, et al. Lung segmentation in chest radiographs using anatomical atlases with nonrigid registration. *IEEE Transactions on Medical Imaging*. 2014; 33(2): 577-590.
- [35] Brown MS, Wilson LS, Doust BD, Gill RW, Sun C. Knowledge-based method for segmentation and analysis of lung boundaries in chest X-ray images. *Computerized Medical Imaging and Graphics*. 1998; 22(6): 463-477.
- [36] Shi F, Wang J, Shi J, Wu ZY, Wang Q, Tang ZY, et al. Review of artificial intelligence techniques in imaging data acquisition, segmentation, and diagnosis for COVID-19. *IEEE Reviews in Biomedical Engineering*. 2021; 14: 4-15.
- [37] Altan A, Karasu S. Recognition of COVID-19 disease from X-ray images by hybrid model consisting of 2D curvelet transform, chaotic salp swarm algorithm and deep learning technique. *Chaos, Solitons & Fractals*. 2020; 140: 110071. Available from: doi: 10.1016/j.chaos.2020.110071.
- [38] Boyat AK, Joshi BK. A review paper: Noise models in digital image processing. *Signal & Image Processing: An International Journal*. 2015; 6(2): 63-75.
- [39] Villar SA, Torcida S, Acosta GG. Median filtering: A new insight. *Journal of Mathematical Imaging and Vision*. 2017; 58(1): 130-146.
- [40] Kirti T, Jitendta K, Ashok S. Poisson noise reduction from X-ray images by region classification and response median filtering. *Sadhana*. 2017; 42(6): 855-863.
- [41] Mehra R. Estimation of the image quality under different distortions. *International Journal of Engineering and Computer Science*. 2016; 5: 17291-17296.
- [42] Davies ER. *Machine Vision* (3rd ed.). 2005.
- [43] Vincent L, Soille P. Watersheds in digital spaces: an efficient algorithm based on immersion simulations. *IEEE Transactions on Pattern Analysis and Machine Intelligence*. 1991; 13(6): 583-598.
- [44] Preim B, Botha C. Image analysis for medical visualization. In: Bernhard Preim, Charl Botha. (eds.) *Visual Computing for Medicine Theory, Algorithms, and Applications* (2nd ed.). Morgan Kaufmann; 2014. p. 111-175.
- [45] Yasin R, Gouda W. Chest X-ray findings monitoring COVID-19 disease course and severity. *Egyptian Journal of Radiology and Nuclear Medicine*. 2020; 51(1):1-18. Available from: doi: 10.1186/s43055-020-00296-x.
- [46] Reyes S, Roche B, Kazzaz F, Ocasionez D, Lal AP, Estrada-Y-Martin RM, et al. Pneumothorax and pneumomediastinum in COVID-19: A case series. *The American Journal of Medical Sciences*. 2020.
- [47] Valette X, duCheyron D, Goursaud S. Mediastinal lymphadenopathy in patients with severe COVID-19. *The Lancet Infectious Diseases*. 2020; 20(11): 1230.
- [48] AdairII LB, Ledermann EJ. Chest CT findings of early and progressive phase COVID-19 infection from a US patient. *Radiology Case Reports*. 2020; 15(7): 819-824.
- [49] M Durrani, Haq IU, Kalsoom U, Yousaf A. Chest X-rays findings in COVID 19 patients at a university teaching hospital-a descriptive study. *Pakistan Journal of Medical Science*. 2020; 36(COVID19-S4): S22-S26.
- [50] Quora. *How much does an X-ray cost in India*. 2021. Available from: <https://www.quora.com/How-much-does-an-X-ray-cost-in-India> [Accessed 16th May 2021].
- [51] The Hindu. *Govt. Caps CT/HRCT scan rate at ₹3000*. 2021. Available from: <https://www.thehindu.com/news/national/andhra-pradesh/govt-caps-cthrct-scan-rate-at-3000/article34408896.ece> [Accessed 16 May 2021].
- [52] Naeem S, Jamil N, Khan HU, Nazir S. Complexity of deep convolutional neural networks in mobile computing.

Complexity In Special issue: Complexity in Deep Neural Networks. 2020.

- [53] Kornilov AS, Safonov IV. An overview of watershed algorithm implementations in open source libraries. *Journal of Imaging*. 2018; 4(10): 123.
- [54] Cordon-Cardo C, Pujadas E, Wajnberg A, Sebra R, Patel G, Firpo-Betancourt A, et al. COVID-19: Staging of a new disease. *Cancer Cell*. 2020; 38(5): 594-597.